Journal of Thermal Analysis and Calorimetry (2020) 141:313–322
https://doi.org/10.1007/s10973-019-09231-3

Numerical calculation and experimental measurement of temperatures and welding residual stresses in a thick-walled T-joint structure

Mato Perić[1] · Sandro Nižetić[2] · Ivica Garašić[3] · Nenad Gubeljak[4] · Tomaž Vuherer[4] · Zdenko Tonković[3]

Received: 29 October 2019 / Accepted: 23 December 2019 / Published online: 4 January 2020

Abstract

In this investigation, a T-joint numerical welding simulation of thick steel plates is performed to estimate transient temperature distributions, residual stress field and model deflections. A sequential simulation method is applied in the numerical simulation, where the thermal analysis is done by using the EBD technique to simulate the weld wire melting and metal filler addition while the mechanical analysis is performed in one step without EBD to shorten the calculation time. Thermocouples, non-destructive X-ray diffraction and semi-destructive hole-drilling methods are used to measure the temperature and residual stress distributions. In the thermal analysis, a simplified heat flux is used which causes a relatively large temperature discrepancy in the weld pool area between the numerical and experimental results. The calculated temperature histories outside the weld pool and its vicinity correlate very well with the experimental measurements with an acceptable discrepancy of approximately 4%. The residual stresses are firstly measured on the model surface without electropolishing and then two times after that, at depths of 0.005 and 0.015 mm. The results of residual stress obtained by numerical modelling and measurement with X-ray agree better when the electropolishing removing layer is set to 0.015 mm, due to a significantly smaller effect of surface conditions that originate from steel plate production.

Keywords Buried-arc welding · T-joint fillet weld · Thermocouples · Residual stresses · X-ray diffraction · Hole-drilling

List of symbols

U	Welding voltage, V
I	Welding current, A
Q	Heat flux, J m^{-3} s^{-1}
v	Welding speed, mm/min
h_c	Convective heat transfer coefficient, W m^{-2} K^{-1}
ε	Surface emissivity factor
η	Welding process efficiency

✉ Mato Perić
mato.peric@fsb.hr

1 Bestprojekt, Bureau of Energetic and Mechanical Engineering Ltd., Petrovaradinska 7, 10000 Zagreb, Croatia

2 LTEF- Laboratory for Thermodynamic and Energy Efficiency, Faculty of Electrical Engineering, Mechanical Engineering and Naval Architecture, University of Split, Ruđera Boškovića 32, 21000 Split, Croatia

3 Faculty of Mechanical Engineering and Naval Architecture, University of Zagreb, I. Lučića 5, 10000 Zagreb, Croatia

4 Faculty of Mechanical Engineering, University of Maribor, Smetanova ulica 17, 2000 Maribor, Slovenia

Abbreviations

MAG	Metal active gas
EBD	Element birth and death

Introduction

Welding is one of the most commonly used procedures for the joining of various structural components in the industry due to its low price and simplicity of performance. During welding, a large localised heat input is introduced to the structure that leads to the melting of the electrode and surrounding base metal. The subsequent rapid cooling of the melted metal after welding causes its non-uniform expansion and contraction. This phenomenon leads to the occurrence of permanent plastic deformations and residual stresses in the welded structure, which has undesirable consequences on the structure integrity, durability, and external appearance and causes dimensional inaccuracies. The removing of these effects through thermal [1, 2] or mechanical procedures [3, 4] requires additional financial expenses and extends the production time. In order to reduce unnecessary costs, it is of prime interest to determine the magnitude of residual stresses and deformations in advance so that appropriate measures can be undertaken to reduce them. Among the numerous forms of welded structures, T-joint fillet welds have a prominent place due to their frequent application. Therefore, in recent years many researchers have been encouraged to research residual stresses and deformations in such types of welded structures. Deng et al. [5] in their study developed a computational procedure and carried out experimental measurements to investigate the impact of the flange thickness on the deflections of a T-joint structure. In their study, it was concluded that that the flange deformations were strongly dependent on the temperature gradient through its thickness. Gannon et al. [6] and Keivani et al. [7] investigated the effect of various welding sequences on residual stress and deflections in a T-joint to determine the best welding path. Li et al. [8] in their numerical simulation introduced a thermo-mechanical interface element to study the weld size, penetration and contact conditions between the T-joint plates and their influence on the sample distortion. Compared with the conventional numerical model, their method showed a better agreement with the experimental measurements. Rong et al. [9] and Perić et al. [10] made welding simulations based on a combination of three-dimensional solid and shell elements to shorten the computation time. Wang et al. [11] dealt with the impact of the gap between the skin plate and stiffener on the residual stress field and deflections in a T-joint. Tian and Luo [12, 13] in their works used both finite element methods and generic algorithms to investigate T-joint deflections after welding. Lostado et al. [14] combined soft computing techniques and the finite element method to optimise the design and reduce the deformations in a T-joint weld. The influence of material property simplifications on the residual stresses and deflections in a T-joint welded steel plate was studied in [15, 16].

It is important to note that all the models described above refer to models welded with the conventional metal active gas (MAG) process, which is very often used in the industry because of its high efficiency, reliability, quality of performance and low manufacture costs. However, due to the increasing demands of the industry for the faster production of welded structures, a high current MAG process (so called buried-arc welding) [17] has been increasingly used in recent years. The main features of this process compared to the conventional one are the increased current and voltage, which results in a higher penetration and melting speed of the welding wire, which greatly accelerates the welding process and reduces the number of welding passes. Due to the smaller number of welding passes, this process is more energy efficient and more environmentally friendly than the conventional MAG welding due to the reduction of CO_2 emissions.

In the authors' previous study [18], a numerical model for residual stress prediction was proposed and experimentally validated on a simple butt-welded plate model. The model was a single pass welded one, where the temperature gradients through the thickness of the plates were small, so as to produce a negligible bending of the welded plates. Here, a detailed comparison of the buried-arc welding procedure against the conventional MAG process was provided. In the present paper, the investigations are further extended to a much more complex model of T-joined welded plates, where the temperature gradients between the upper and lower surfaces of the horizontal plate are large causing their significant bending. The T-joint model is welded in two single passes and the cooling time between the passes is taken into account in the numerical model. It is important to point out that according to these authors, there have not been any numerical or experimental available investigations on T-joint structures welded with a buried-arc welding procedure.

This paper has five sections. In the second section, the experimental set-up and methods for measuring temperature, deformations and residual stresses are described. The numerical model description is shown in the third section. All the needed comparisons of the measured and numerically obtained values of temperatures, deflections and residual stresses are provided in the fourth section. The main conclusions of the investigation are given in the last section.

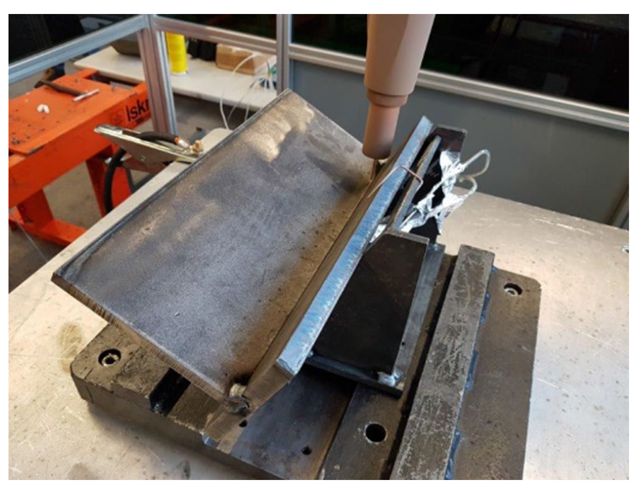

Fig. 1 Experimental set-up of two T-joint welded plates

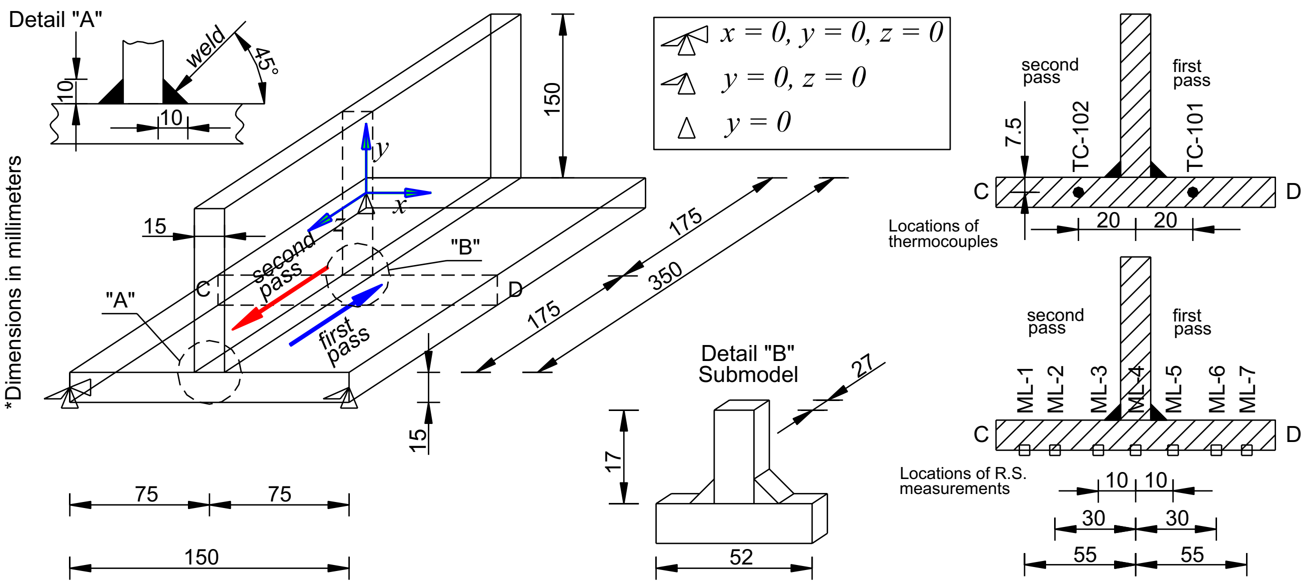

Fig. 2 Dimensions of T-joint welded plates

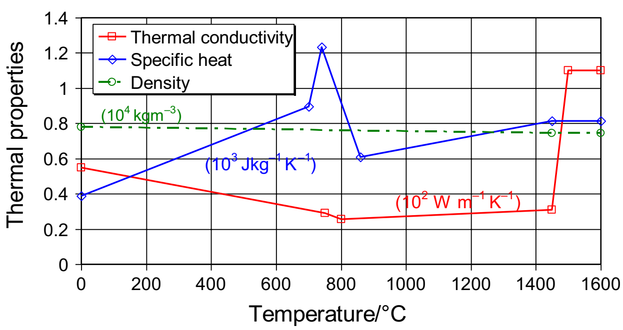

Fig. 3 Thermal properties of S355J2+N steel [19]

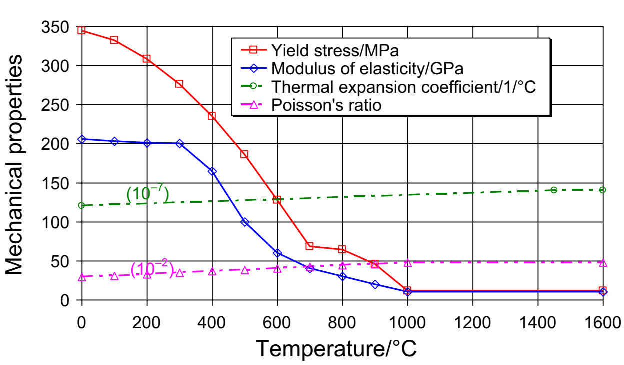

Fig. 4 Mechanical properties of S355J2+N steel [19]

Experimental set-up and measurements

Main welding conditions

The sample consisted of two 15 mm thick plates, each of dimensions of 350 mm × 150 mm (Figs. 1 and 2), that are welded into a T-joint in two single passes with the buried-arc welding procedure. The material of the plates is non-alloyed low-carbon steel S355J2+N. The temperature-dependent thermal and mechanical properties, including the chemical composition, are given in Figs. 3, 4 and Table 1, respectively. Before the beginning of the welding process, the plates are secured with tack welds at the start/end of the sample so that the joint is performed with a negligible small gap between them. The plates are welded free, without any mechanical fixtures. The welding is completed in two passes; first on the one side and then on the other side after the rotation of the sample. The material transfer is very stable with no significant arc interruptions or spattering. The diameter of the welding wire is 1.6 mm, and the classification is in accordance with ISO14341- A:G 42 4 C/M G3Si1. The elapsed cooling time between the two passes is 352 s.

Having the welding procedure completed, the visual testing in accordance with ISO 17637 is conducted whereby no surface imperfections are observed. In Table 2, the main welding parameters from this experiment are summarised.

Table 1 Chemical composition of S355 J2 + N steel (mass %) [18]

C	Si	Mn	P	S	N	Cu	Cr	Ni	Mo	Al	V	Ti	Nb
0.17	0.24	1.25	0.016	0.006	0.008	0.23	0.06	0.1	0.11	0.0032	0.005	0.025	0.033

Table 2 Main welding parameters

Welding current I	Welding voltage U	Welding speed v	Wire diameter	Wire feed speed	Shielding gas composition	Shielding gas flow
540 A	41 V	404 mm/min	1.6 mm	10.6 m/min	100% CO_2	25 L/min

Fig. 5 Residual stress measurement using Pulstec μ-X360 device

Measurements of temperatures, deflections and residual stresses

To measure the temperature responses from the beginning of the welding until cooling to the ambient temperature (25 °C), two NiCr-Ni Inconel 600 sheathed thermocouples of type K, named as TC-101 and TC-102, are mounted inside the horizontal plate at a depth of 7.5 mm measured from the bottom surface (Fig. 2, line C–D). The selected thermocouples have the ability to measure temperatures between −220 and 1150 °C with an acceptable measurement error of 1.5%. A data logger (from PICO Technology Ltd.) is used to transfer the measured data from the thermocouples to the computer.

The measurement of the horizontal plate deflections after welding and cooling time to the ambient temperature is conducted using a Vernier calliper at the bottom side along line C–D marked in Fig. 2. This measurement is performed with respect to a plane made up of three points in which the vertical displacement is zero ($y=0$), as shown in Fig. 2. These three points represent the fixation nodes in the numerical mechanical analysis.

To measure the residual stress, the non-destructive X-ray diffraction cosα-method [20, 21] is employed by using a portable device Pulstec μ-X360 (from Pulstec Industrial Co. Ltd., Fig. 5). The first measurement is conducted on an unpolished T-joint model. After that the electropolishing procedure is performed in order to avoid the influence of the surface state effect formed during the thermo-mechanical processing of the steel plates on the accuracy of the results whereby the measurements are performed at 0.005 mm and 0.015 mm depths. Since the depth of the electropolishing depends on the initial surface state, a lack of data might occur because of absorbed scattered X-rays towards the sensor by the material that is not electropolished. Here, the electropolishing procedure is performed by using an EP-3 device (from Pulstec Industrial Co. Ltd.). To determine the required depth of the electropolishing, a step-by-step removal of the surface material is done to expose the underneath layers to the X-rays. The residual stresses are measured on seven locations named from ML-1 to ML-7 (Fig. 2, line C–D) on the bottom surface of the T-joint.

In order to verify the obtained results with X-ray measurements, the residual stresses are additionally checked by applying the hole-drilling method of stress relaxation which is widely used in the industry. The measurements are conducted on ML-1 and ML-2 locations (Fig. 2, coordinates $x=20$ mm and $x=45$ mm) at the bottom surface of the T-joint sample. The procedure is performed following the ASTM E837 standard. A Vishay RS200 device (from Vishay Precision Group) and Hottinger rosettes of type 1,5/120 RY 61 (from Hottinger Baldwin Messtechnik GmbH) are used in this experiment.

Finite element simulation

The welding simulation in this study is carried out by using a sequential modelling approach, e.g. by conducting a nonlinear heat transfer analysis firstly followed by using the obtained thermal field as input load in the mechanical analysis using Abaqus/Standard software. Due to the lack of data regarding a heat flux definition for a buried-arc welding procedure in the literature, a simplified heat flux definition is used in the thermal analysis. Here, it is assumed that the total heat input to the weld bead takes place via melting droplets, and that the heat flux is uniformly distributed over the weld volume whereby it is calculated according to Eq. (1):

$$Q = \frac{\eta UI}{V_H} \quad (1)$$

In Eq. (1), η denotes the efficiency of the welding process, while U, I and V_H are the welding voltage, welding current and heat source volume, respectively. In the authors' previous work [18], the buried-arc welding process efficiency was investigated using a parametric analysis whereby this value is estimated to be approximately 85%. Considering the welding voltage and welding current values from Table 2 with the assumption of the process efficiency being 85%, the heat flux introduced to the weld is $Q=5.59\times10^{10}$ J m^{-3} s^{-1}. On the outer surfaces of the welded model, the temperature-independent convective heat transfer coefficient ($h_c=10$ W m^{-2} K^{-1}) and emissivity ($\varepsilon=0.9$) are assumed. In the heat transfer analysis, the movement of the electrode and addition of weld filler are simulated by applying the element birth and death (EBD) technique. For the purpose of simulating the moving of the electrode, the weld bead is divided into 104 element sets, each of 6.731 mm in length. By applying the model change option available in Abaqus/Standard software, all sets are virtually removed (element death) from the model in the first step of the numerical simulation. The element sets are then added (element birth) step-by-step, simulating the moving of the electrode. In each step, every element set is initially added and the heat flux is imposed on it afterwards. The duration of heat flux adding for each individual element set is 1 s. Having added all 104 element sets, the welding process then ends. The final step is the cooling process and the time is set to 7500 s. For the purpose of thermal transient analysis, the T-joint model is discretized using DC3D8 elements, which are three-dimensional eight-node linear hexahedral elements with a full integration scheme from the Abaqus library. The mechanical analysis is performed simultaneously in only one step, without EBD application to shorten the computation time [22, 23]. The base and weld wire metals are considered isotropic and homogeneous elastic-perfectly plastic solids that yield in accordance with the von Mises criterion and the associated flow rule [24–26]. The nonlinear material behaviour is modelled by applying incremental plasticity and geometrically nonlinear behaviour of plates. As it is shown in the literature [27], there is no need to take the phase transformations into account in the case of low-carbon steel welding due to its small impact on the residual stress field and deformations. Furthermore, the creep of the material is neglected as the high-temperature cycles during the welding last very short. To overcome locking issues, the T-joint is discretized in the mechanical analysis by the eight-node hexahedral elements C3D8I enhanced by incompatible modes, which are an improved version of the first-order C3D8 elements. The plates are free welded, also without mechanical fixtures, but in the mechanical analysis, the fixtures are added only to disable the possibility of structure motion as a rigid body. Since the initial gap between the plates is very small and the plates are tack-welded before the beginning of the welding process, the horizontal plate and vertical plate are modelled as a single unit, so that the influence of the small gap on the final residual stress and deflections are neglected in this study. The flow chart for the sequentially coupled thermo-mechanical analysis is shown in Fig. 6.

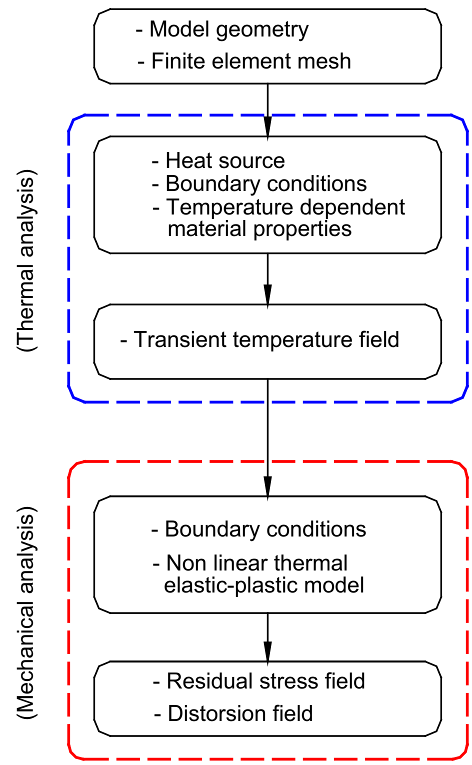

Fig. 6 Flow chart of sequentially modelling approach

Due to a lack of data regarding the thermo-physical and mechanical properties of the weld wire material, they are assumed as base metal ones. A more detailed explanation of the numerical model is provided in the authors' previous work [28].

The T-joint sample finite element mesh consisting of 14,456 finite elements is presented in Fig. 7. A very dense mesh is modelled in the weld pool and in the surrounding areas, while in the areas far away from the weld, where the thermal gradients are smaller, a coarser mesh is used in order to reduce the total number of elements. To check the mesh sensitivity, the submodeling technique [29, 30] is applied on a small part of dimensions $52\times27\times17$ mm^3 (Figs. 2 and 7) with a very dense mesh that is extracted from the full global T-joint model. The number of finite elements of the submodel is 15,740, and the element types are the same as in the full global T-joint sample. The deviations in temperature, deflections and residual stresses between the

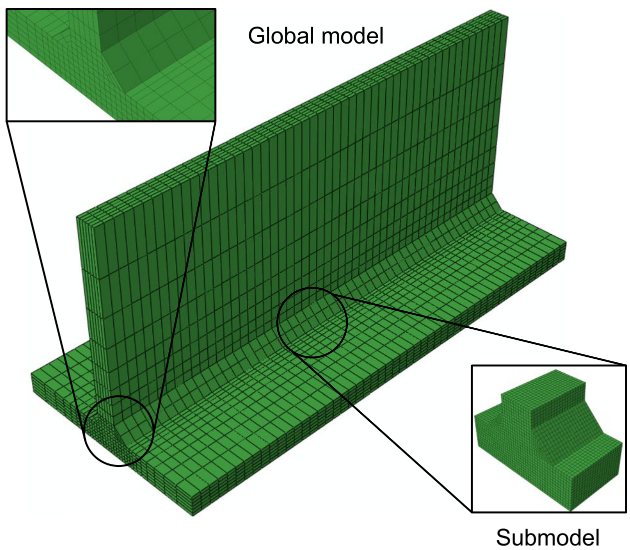

Fig. 7 T-joint sample mesh of finite elements

full global T-joint model and submodel are under 1% and it is concluded that the mesh of the T-joint model is properly designed.

Results and discussions

Thermal analysis

A comparison of numerically obtained and measured temperature histories at location TC-101 for the first 800 s after the start of welding is presented in Fig. 8. It can be noted that during the first passing of the electrode, the temperature difference between the numerically calculated and experimentally obtained peak values is about 30%. This is because the thermocouple is set too close to the source of heat and the simplified model presented in the numerical analysis cannot fully describe the temperature distribution in the weld pool and its vicinity. Very quickly after passing the first electrode, the difference between the numerically obtained and experimentally measured temperatures vanishes and it drops to less than 1% before the beginning of the second pass. At the second passage of the electrode, the difference in the experimentally measured and numerically obtained peak temperatures is less than 3% since the thermocouple TC-101 is now far ahead of the heat source, much more than at the first passage of the electrode. Approximately the same temperature difference of 3% remains in the cooling process to the ambient temperature.

Figure 9 shows the numerically and experimentally obtained histories at location TC-102 for the first 800 s after the start of the welding process. During the first passing of the electrode, the obtained difference between the numerically calculated and experimentally obtained temperatures are less than 4% because the thermocouple is far from the heat source. During the second pass, the electrode is again very close to the thermocouple and the approximate difference between the experimentally and numerically measured temperatures is 35%. The cooling curves for 481 s and 530 s after the welding start (Fig. 2, line C–D), together with the experimentally measured values, are plotted in Fig. 10, while full-field temperature distributions for the 481 s and 530 s after the welding process beginning are shown in Fig. 11.

Mechanical analysis

Figure 12 shows the T-joint deflection profile at the bottom surface of the welded sample (Fig. 2, line C–D) after the welding process and cooling to the ambient temperature and is plotted together with the measured values. Here, it is obvious that the measured and calculated deflection values correspond very well, and the maximum difference is about 15%. The maximum numerically calculated horizontal plate deflection reaches 1.8 mm. Also, a considerable

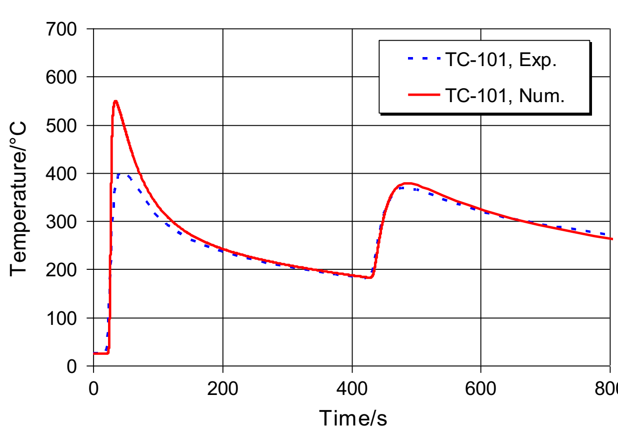

Fig. 8 Temperature-time histories at node TC-101

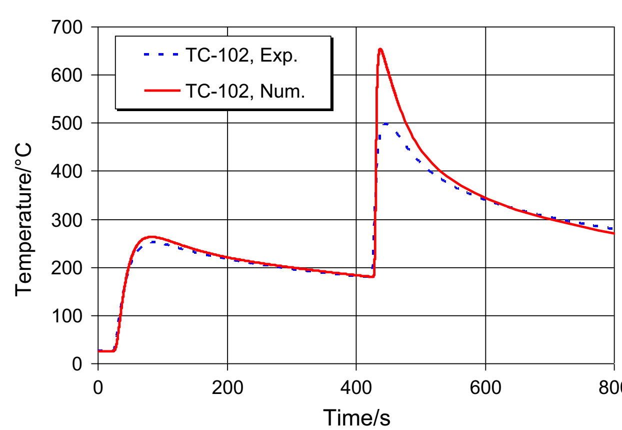

Fig. 9 Temperature-time histories at node TC-102

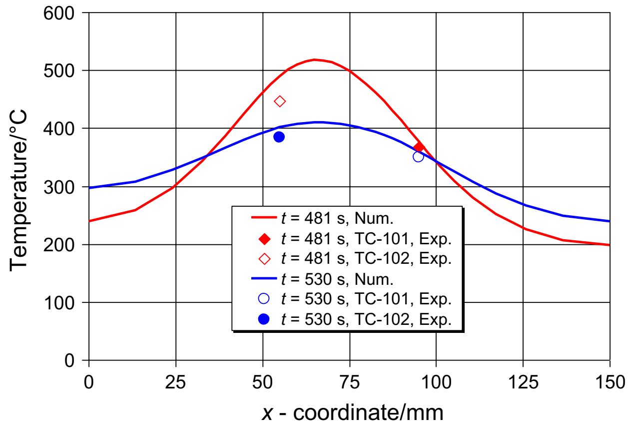

Fig. 10 Cooling curves for 481 s and 530 s after beginning of welding process (Fig. 2, line C-D)

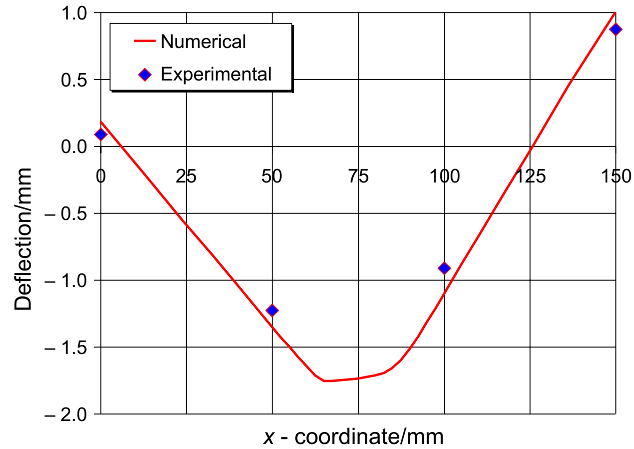

Fig. 12 Deflection curve at model bottom surface (Fig. 2, line C–D)

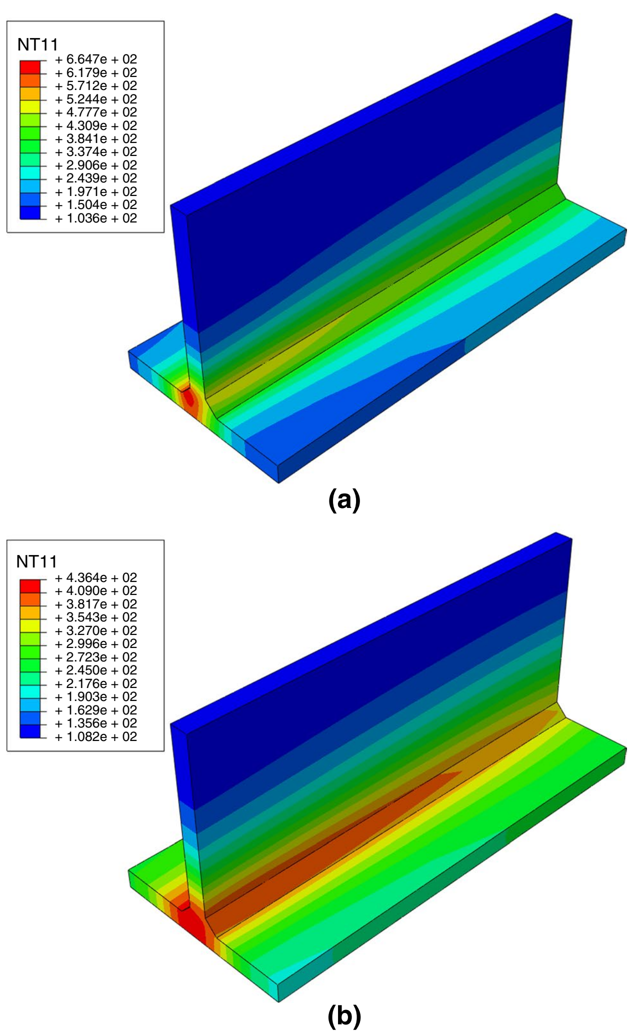

Fig. 11 Transient temperature field: **a** 481 s after beginning of welding process, **b** 530 s after beginning of welding process

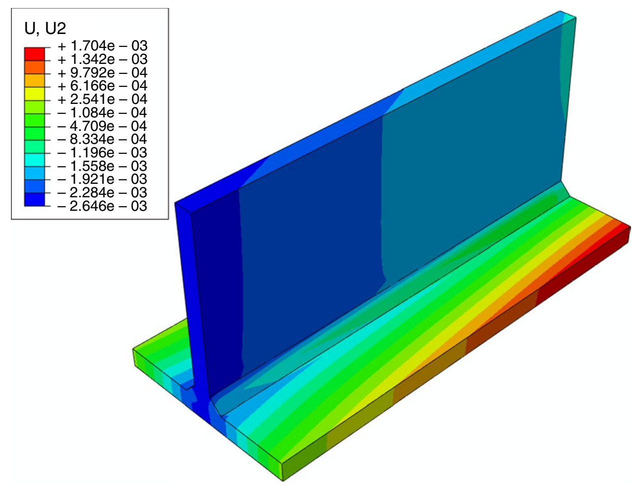

Fig. 13 Deflection distribution field in *y*-direction

deformation of the structure is apparent due to torsion which can be attributed to very intense melting due to high heat input. The full-field deflection distribution in *y*-direction is shown in Fig. 13.

Figures 14 and 15 show the measured longitudinal (parallel to the welding path) and transversal (perpendicular to the welding path) residual stresses in seven points along line C–D (Fig. 2) obtained with X-ray diffraction. As earlier mentioned, at each point, the residual stresses are first measured without electropolishing. The stresses are then measured again with the use of electropolishing procedures at depths of 0.005 mm and 0.015 mm. As seen in the figures before electropolishing in both longitudinal and transversal directions, the compressive residual stresses are measured at each of the seven measuring points. This clearly indicates the significant impact of initial residual stresses originating from the previous fabrication process. These stresses could be removed through the annealing procedure at high

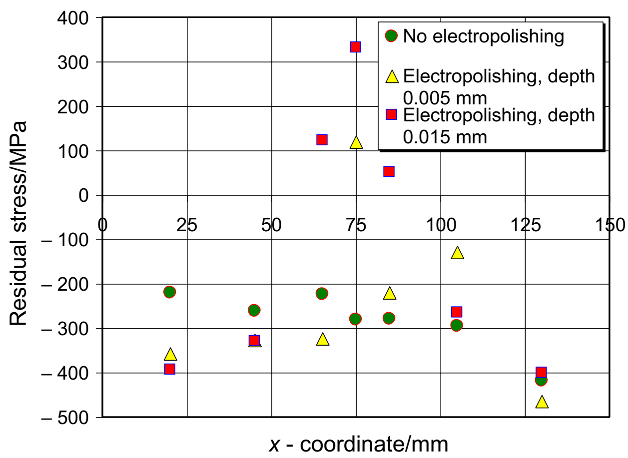

Fig. 14 Longitudinal residual stress (Fig. 2, line C–D) obtained with X-ray diffraction at several electropolishing depths

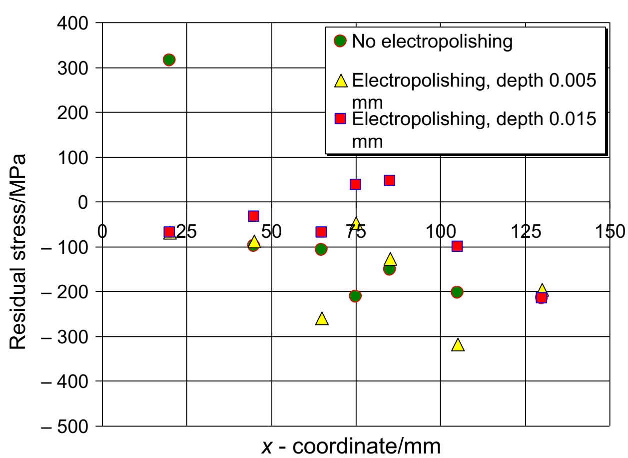

Fig. 15 Transversal residual stress (Fig. 2, line C–D) obtained with X-ray diffraction at several electropolishing depths

temperatures before the beginning of welding, but unfortunately this is not performed in this case. After the first electropolishing at a depth of 0.005 mm, the values of the longitudinal residual stresses generally shift to lower compressive stresses at the same points, while in the middle (coordinate $x = 75$ mm), the longitudinal residual stress reaches a tensile value.

In the case of residual stresses in the transversal direction, the residual stress measurements at these same points swing, to higher values in the middle and to even lower compressive stresses away from the weld area.

Finally, after the second electropolishing, both longitudinal and transversal tensile stresses are obtained at a depth of 0.015 mm in the centre of the plate ($x = 75$ mm), while at the end of the plates they remain compressive.

The comparison of the longitudinal residual stress distribution (Fig. 2, line C–D) obtained by the numerical

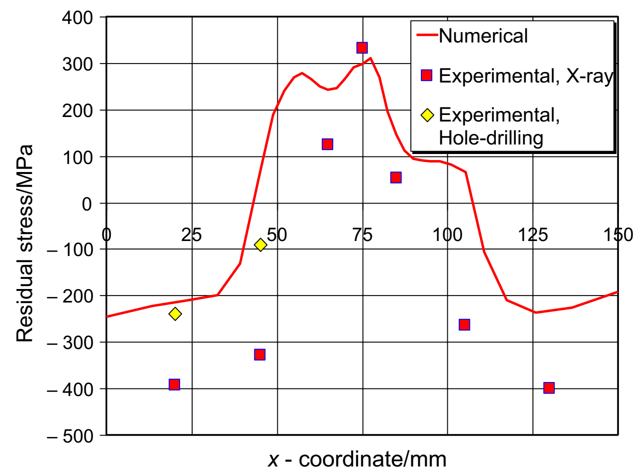

Fig. 16 Longitudinal residual stress distribution (Fig. 2, line C–D) obtained by numerical simulation, X-ray diffraction and hole-drilling method

simulation, X-ray diffraction at a depth of 0.015 mm and hole-drilling method is presented in Fig. 16. Generally speaking, the measured longitudinal residual stresses with X-ray diffraction follow well the trend of the curve obtained by the numerical simulation. The maximum longitudinal stress measured with X-ray diffraction at the coordinate $x = 75$ mm is tensile and reaches 332 MPa which is close to the yield stress of the base material. Other longitudinal stresses in the weld vicinity in both the numerical analysis and experimental procedure are tensile, as well. Looking at the horizontal plate ends, it is seen that the longitudinal stresses change from tensile to compressive, which is confirmed by both simulation and experimental measurements. It is concluded that longitudinal tensile stresses only govern the weld and its close regions, while further away from the weld they become compressive.

The transversal residual stress distribution (Fig. 2, line C–D) obtained by the numerical simulation, X-ray diffraction at a depth of 0.015 mm and hole-drilling method is presented in Fig. 17. It is obvious that as with the longitudinal stresses, the trends of the numerical simulation and experimental measurements match very well.

Finally it can be stated, the trend of the longitudinal and transversal residual stresses measured at ML-1 and ML-2 locations by applying the hole-drilling method correlates well with the results of the numerical calculations. Both experimental methods show compressive longitudinal and compressive transversal stresses at locations ML-1 and ML-2.

The numerical obtained longitudinal and transversal full-field residual stress distributions are shown in Figs. 18 and 19.

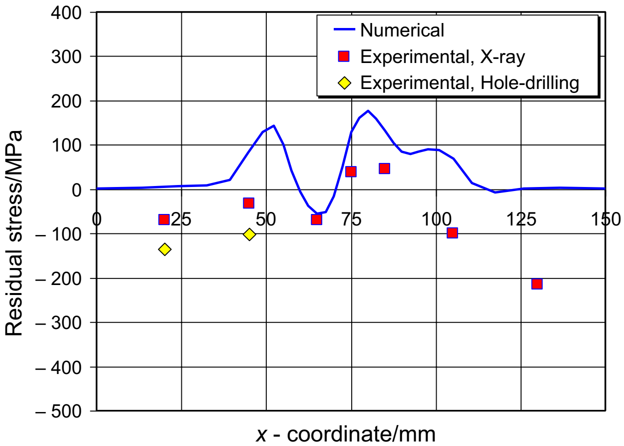

Fig. 17 Transversal residual stress distribution (Fig. 2, line C–D) obtained by numerical simulation, X-ray diffraction and hole-drilling method

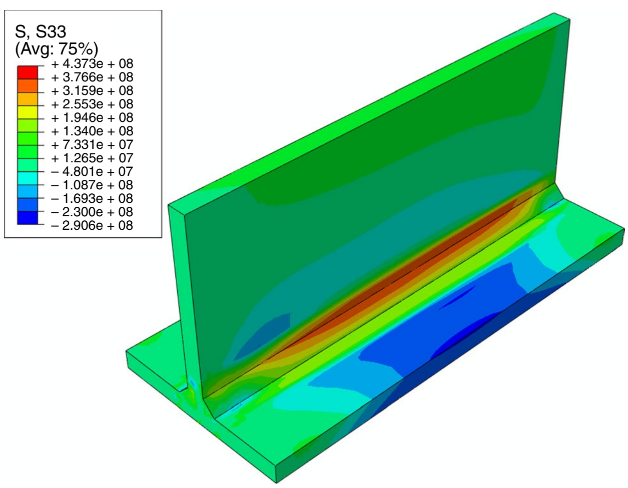

Fig. 18 Longitudinal residual stress field

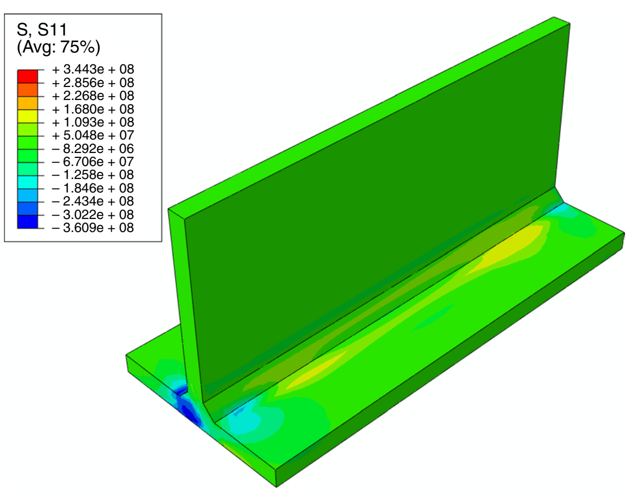

Fig. 19 Transversal residual stress field

Conclusions

In this work, a numerical simulation is done to investigate the temperature transient temperature distributions in the welding and cooling processes, residual stress distributions and plate deflections in a T-joint welded structure. The plates are welded by using a high current buried-arc welding technique. The thermal analysis is performed with a heat flux simplification and by applying the EBD technique to simulate the moving of the welding torch. The mechanical analysis is conducted in one step only, without the EBD application and the main conclusions of the work are as follows:

- The presented simplified model can describe temperature distributions very well throughout the structure except in the weld pool and areas very close to the weld pool. The measured temperatures outside the weld pool are in very good correlation with the experimentally measured values.
- The presented numerical model gives a very realistic deflection distribution of a T-joint fillet welded structure. The difference between the numerically calculated and experimentally measured values is below 15%.
- The measured longitudinal and transversal residual stresses with both X-ray diffraction and hole-drilling method are in very good correlation with the numerically predicted values and the deviations can be attributed to the initial residual stresses that originate from steel plate production.

As a general conclusion, it can be noted that despite the applied heat flux simplification in the thermal analysis and neglecting the EBD method in the mechanical analysis, the presented numerical model could be an acceptable solution for residual stresses and deflections calculations not only for simple butt-welded structures, but also for geometrically more complex structures like T-joints, which are welded with the buried-arc welding procedure.

Acknowledgements Authors acknowledge Marijana Milković, M.Sc. ME., for performing residual stress measurements and the Slovenian Research Agency for founding the research program P2-0137 Numerical and Experimental Analysis of Nonlinear Mechanical Systems.

References

1. Takazawa H, Yanagida N. Effect of creep constitutive equation on simulated stress mitigation behavior of alloy steel pipe during post-weld heat treatment. Int J Press Vessels Pip. 2014;117–118:42–8. https://doi.org/10.1016/j.ijpvp.2013.10.008.
2. Perić M, Garašić I, Nižetić S, Dedić-Jandrek H. Numerical analysis of longitudinal residual stresses and deflections in a T-joint

welded structure using a local preheating technique. Energies. 2018;11(12):3487. https://doi.org/10.3390/en11123487.
3. Coules HE, Colegrove P, Cozzolino LD, Wen SW. High pressure rolling of low carbon steel weld seams: part 1—effects on mechanical properties and microstructure. Sci Technol Weld Join. 2013;18(1):63–78. https://doi.org/10.1179/1362171812Y.0000000079.
4. Coules HE, Colegrove P, Cozzolino LD, Wen SW, Kelleher JF. High pressure rolling of low carbon steel weld seams: part 2—roller geometry and residual stress. Sci Technol Weld Join. 2013;18(1):84–90. https://doi.org/10.1179/1362171812Y.0000000080.
5. Deng D, Liang W, Murakawa H. Determination of welding deformation in fillet-welded joint by means of numerical simulation and comparison with experimental measurements. J Mater Process Technol. 2007;183:219–25. https://doi.org/10.1016/j.jmatprotec.2006.10.013.
6. Gannon L, Liu Y, Pegg M, Smith M. Effect of welding sequence on residual stress and distortion in flat-bar stiffened plates. Effect of welding-induced residual stress and distortion on ship hull girder ultimate strength. Mar Struct. 2010;23(3):375–404. https://doi.org/10.1016/j.marstruc.2010.05.002.
7. Keivani R, Jahazi M, Pham T, Khodabandeh AR, Afshar MR. Predicting residual stresses and distortion during multisequence welding of large size structures using FEM. Int J Adv Manuf Technol. 2014;73(1–4):409–19. https://doi.org/10.1007/s00170-014-5833-4.
8. Li Y, Wang K, Jin Y, Xu M, Lu H. Prediction of welding deformation in stiffened structure by introducing thermo-mechanical interface element. J Mater Process Technol. 2015;216:440–6. https://doi.org/10.1016/j.jmatprotec.2014.10.012.
9. Rong Y, Zhang G, Huang Y. Study of welding distortion and residual stress considering nonlinear yield stress curves and multi-constraint equations. J Mater Eng Perform. 2016;25(10):4484–94. https://doi.org/10.1007/s11665-016-2259-1.
10. Perić M, Tonković Z, Rodić A, Surjak M, Garašić I, Boras I, Švaić S. Numerical analysis and experimental investigation of welding residual stresses and distortions in a T-joint fillet weld. Mater Des. 2014;53:1052–63. https://doi.org/10.1016/j.matdes.2013.08.011.
11. Wang C, Kim YR, Kim JW. Comparison of FE models to predict the welding distortion in T-joint gas metal arc welding process. Int J Adv Manuf Technol. 2014;18(8):1637–931. https://doi.org/10.1007/s12541-014-0513-8.
12. Tian L, Luo Y. A comparison study of BPN and SVM prediction models for inherent deformations of T-welded joints. Mech Adv Mater Struct. 2019. https://doi.org/10.1080/15376494.2019.1567881 **(in press)**.
13. Tian L, Luo Y. A study on the prediction of inherent deformation in fillet–welded joint using support vector machine and genetic optimization algorithm. J Intell Manuf. 2019. https://doi.org/10.1007/s10845-019-01469-w **(in press)**.
14. Lostado R, Fernandez Martinez R, Mac Donald BJ, Villanueva PM. Combining soft computing techniques and the finite element method to design and optimize complex welded products. Integr Comput-Aid E. 2015;22(2):153–70. https://doi.org/10.3233/ICA-150484.
15. Bhatti AA, Barsoum Z, Murakawa H, Barsoum I. Influence of thermo-mechanical material properties of different steel grades on welding residual stresses and angular distortion. Mater Des. 2015;65:878–89. https://doi.org/10.1016/j.matdes.2014.10.019.
16. Perić M, Tonković Z, Garašić I, Vuherer T. An engineering approach for a T-joint fillet welding simulation using simplified material properties. Ocean Eng. 2016;128:13–21. https://doi.org/10.1016/j.oceaneng.2016.10.006.
17. Baba H, Era T, Ueyama T, Tanaka M. Single pass full penetration joining for heavy plate steel using high current GMA process. Weld World. 2017;61(5):963–9. https://doi.org/10.1007/s40194-017-0464-7.
18. Perić M, Garašić I, Tonković Z, Vuherer T, Nižetić S, Dedić-Jandrek H. Numerical prediction and experimental validation of temperature and residual stress distributions in buried-arc welded thick plates. Int J Energy Res. 2019;43(8):3590–600. https://doi.org/10.1002/er.4506.
19. Pilipenko A. Computer simulation of residual stress and distortion of thick plates in multi-electrode submerged arc welding. Their mitigation techniques. Doctoral Thesis, Trondheim, 2001.
20. Huang H, Tsutsumi S, Wang J, Li L, Murakawa H. High performance computation of residual stress and distortion in laser welded 301L stainless sheets. Finite Elem Anal Des. 2017;135:1–10. https://doi.org/10.1016/j.finel.2017.07.004.
21. Lin J, Ma N, Lei Y, Murakawa H. Measurement of residual stress in arc welded lap joints by cosα X-ray diffraction method. J Mater Process Technol. 2017;243:387–94. https://doi.org/10.1016/j.jmatprotec.2016.12.021.
22. Perić M, Tonković Z, Karšaj I, Stamenković D. A simplified engineering method for a T-joint welding simulation. Therm Sci. 2018;22(3):S867–73. https://doi.org/10.2298/TSCI171108020P.
23. Seleš K, Perić M, Tonković Z. Numerical simulation of a welding process using a prescribed temperature approach. J Constr Steel Res. 2018;145:49–57. https://doi.org/10.1016/j.jcsr.2018.02.012.
24. Venkatkumar D, Ravindran D. Effect of boundary conditions on residual stresses and distortion in 316 stainless steel butt welded plate. High Temp Mater Proc. 2019;38:827–36. https://doi.org/10.1515/htmp-2019-0048.
25. Nasouri R, Nguyen K, Montoya A, Matamoros A, Bennett C, Li J. Thermally-induced demands due to hot dip galvanization of high mast illumination poles. Part I: finite element model development. J Constr Steel Res. 2019;162:105705. https://doi.org/10.1016/j.jcsr.2019.105705.
26. Zhang J, Yu L, Liu Y, Ma Z, Li H, Liu C, Wu J, Ma J, Li Z. Analysis of the effect of tungsten inert gas welding sequences on residual stress and distortion of CFETR vacuum vessel using finite element simulations. Metals-Basel. 2018;8(11):912. https://doi.org/10.3390/met8110912.
27. Deng D. FEM prediction of welding residual stress and distortion in carbon steel considering phase transformation effects. Mater Des. 2009;30(2):359–66. https://doi.org/10.1016/j.matdes.2008.04.052.
28. Perić M, Seleš K, Tonković Z, Lovrenić-Jugović M. Numerical simulation of welding distortions in large structures with a simplified engineering approach. Open Phys. 2019;17:719–30. https://doi.org/10.1515/phys-2019-0076.
29. Perić M, Tonković Z, Maksimović SK, Stamenković D. Numerical analysis of residual stresses in a T-joint fillet weld using a submodeling technique. FME Trans. 2019;47(1):183–9. https://doi.org/10.5937/fmet1901183P.
30. Marenić E, Skozrit I, Tonković Z. On the calculation of stress intensity factors and J-integrals using the submodeling technique. J Press Vessel-Technol ASME. 2010;132(4):041203. https://doi.org/10.1115/1.4001267.